LANGMUIR

pubs.acs.org/Langmuir Article

Cancer-Associated Gangliosides as a Therapeutic Target for Host Defense Peptide Mimics

Michael W. Martynowycz, Konstantin Andreev, Amram Mor, and David Gidalevitz*

Cite This: *Langmuir* 2023, 39, 12541−12549 Read Online

ACCESS | Metrics & More | Article Recommendations | Supporting Information

ABSTRACT: Aberrant levels of glycolipids expressed on cellular surfaces are characteristic of different types of cancers. The oligomer of acylated lysine (OAK) mimicking antimicrobial peptides displays in vitro activity against human and murine melanoma cell lines with upregulated GD3 and GM3 gangliosides. Herein, we demonstrate the capability of OAK to intercalate into the sialo-oligosaccharides of DPPC/GD3 and DPPC/GM3 lipid monolayers using X-ray scattering. The lack of insertion into monolayers containing phosphatidylserine suggests that the mechanism of action by OAKs against glycosylated lipid membranes is not merely driven by charge effects. The fluorescence microscopy data demonstrates the membrane-lytic activity of OAK. Understanding the molecular basis for selectivity toward GD3 and GM3 gangliosides by antimicrobial lipopeptides will contribute to the development of novel therapies to cure melanoma and other malignancies.

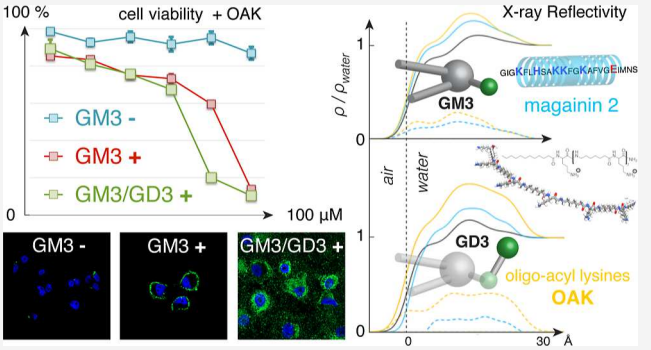

INTRODUCTION

Gangliosides are a structurally and functionally diverse group of glycosphingolipids that contain one or more sialic acid groups. They are abundantly present at the outer leaflet of eukaryotic plasma membranes and engaged in multiple physiological processes including cell−cell recognition and adhesion, ion homeostasis, and immune signaling.[1] The expression patterns of gangliosides vary significantly between different species and tissues, throughout embryogenesis, and under pathological conditions.[2] Disialoganglioside with three glycosyl groups (GD3) and its monosialyl precursor (GM3) have been reported to constitute 80% of the total surface lipid-bound sialic acids in metastatic melanomas.[3]

Oligo-acyl-lysines (OAKs) are peptide mimetic compounds that incorporate variable hydrocarbon chains to positively charged lysine residues through carbonyl groups (Figure 1b).[4] Originally recognized for their antibacterial and antimalarial properties,[5−7] OAKs have been more recently reported to suppress prostate adenocarcinoma growth both in vitro and in vivo.[8]

We propose a mechanism of membrane disruptive activity on model melanoma membranes by OAKs by intercalating them into sialic acids of GD3 and GM3 gangliosides (Figure 1a), distinct from merely electrostatic interactions with anionic phospholipids in bacteria.[9] To test this hypothesis, we reconstitute Langmuir monolayers composed of either GD3 or GM3 mixtures with dipalmitoyl-*sn*-glycero-3 phosphatidylcholine (DPPC) in physiologically relevant proportions mimicking the melanoma cell surface.[10] The insertion of octameric OAK, dodecanoyllysyl-hepta(aminooctanoyllysyl)-amide (C_{12}K-7α8) from the aqueous subphase into model lipid membranes is probed using constant-pressure insertion assays and X-ray reflectivity.[11] Monolayers of DPPC mixed with saturated dipalmitoyl-phosphatidylserine (DPPS) are employed to characterize OAK interactions with anionic phospholipids.[12] Although other lipids are negatively charged, such as dipalmitoyl-*sn*-glycero-3-phosphoglycerol (DPPG), DPPS was chosen since it occurs in higher abundance in human cells and has been implicated in other important physiological processes.[13,14] DPPG is often used as a model system for bacterial cell membranes.[15] Langmuir monolayers mimic the outer leaflet of a cell where the aqueous environment below acts as a platform to introduce membrane active compounds to the simplified lipid monolayer.[16] X-ray reflectivity is used to generate an electron density profile of the monolayer film before and after the compounds are introduced. By combining the insertion assay with the changes in electron density, an idea of how the compounds interact with the lipids can be deduced. In vitro cytotoxicity is measured on human cervical (HeLa) and lung (A549)

Received: April 14, 2023
Revised: July 31, 2023
Published: August 30, 2023

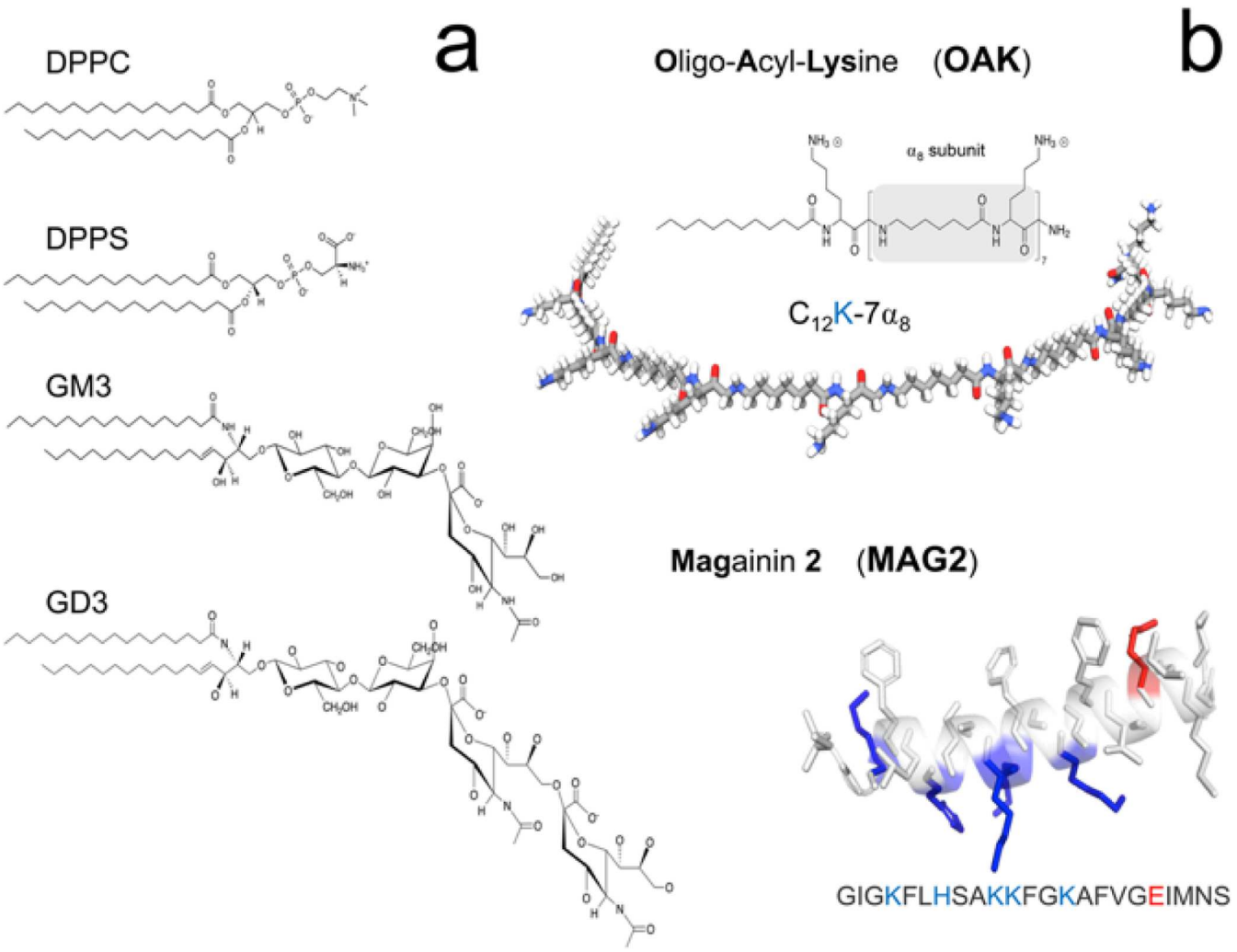

Figure 1. Chemical structures of lipids (a) and antimicrobials (b) used in this study. Brackets dictate α8 (aminooctanoyl-lysyl) subunits (gray).

carcinoma and human (SK-MEL-28) and murine (B78) melanoma cell lines. Non-cancerous Chinese hamster ovary (CHO-K1) cells and primary embryonic chicken fibroblasts (UMNSAH/DF-1) are used as positive and negative controls, respectively. Ganglioside surface levels are detected by immunostaining using anti-GD3 and anti-GM3 monoclonal antibodies. The data are compared to those by antimicrobial peptide magainin 2 (MAG2) (Figure 1b), which has been previously shown to suppress proliferation and induce cytolysis of tumor cells.[17]

EXPERIMENTAL SECTION

Cells and Antimicrobials. *HeLa* (CCL-2), A549 (CCL-185), CHO-K1 (CCL-61), and primary chicken embryonic fibroblasts UMNSAH/DF-1 (CRL-12203) along with Kaighn's Modification of Ham's F-12 Medium (F-12K) (30-2004) and Eagle's minimum essential medium (EMEM) (30-2003) were obtained from the American Tissue Culture Collection (Maryland, USA). Human SK-MEL-28 melanoma was a generous gift by Dr. Leonidas C. Platanias (Robert H. Lurie Comprehensive Cancer Center of Northwestern University, Chicago, IL). B78 cells were kindly provided by Dr. Gary H. Cohen (University of Pennsylvania, Philadelphia, PA). Fetal bovine serum (FBS) was purchased from Gemini Bio Products (West Sacramento, CA), and 96-well clear bottom plates (Costar) were obtained from Corning Inc. (Corning, NY). The Alamar Blue cell viability assay kit and Dulbecco's modified Eagle's medium (DMEM, Gibco) were obtained from Thermo Fisher Scientific (Waltham, MA). Magainin 2 was purchased from AnaSpec (Fremont, CA), and lipids were obtained from Avanti Polar Lipids (Alabaster, AL) and were used without further purification.

OAK Synthesis. C_{12}K-7α8 derivative of of ϵ-poly-L-lysine was synthesized by the solid-phase method by applying the 9-fluorenylmethyloxy carbonyl (Fmoc) active ester chemistry (Peptide Synthesizer model 433A; Applied Biosystems, Waltham, MA) as previously described.[7] In brief, 4-methylbenzhydrylamine resin was used to obtain amidated compounds. The crude compounds were purified to chromatographic homogeneity in the range of >95% by reverse-phase high-performance liquid chromatography (HPLC) on a Vydac C18 column (Grace, Columbia, MD) with a linear gradient of acetonitrile in water (1%/min); both solvents contained 0.1% trifluoroacetic acid. The purified compounds were analyzed by mass spectrometry (Alliance HPLC, Waters, Milford, MA) to confirm their compositions and stored as lyophilized powders at −20 °C. The stock solutions were prepared in ultrapure water (Millipore Sigma, Burlington, MA), briefly vortexed, sonicated, and centrifuged, followed by dilution in the appropriate medium.

Cytotoxicity Assays. In vitro cytotoxicity of MAG2 and OAK was assessed via an Alamar Blue (resazurin) cell viability assay kit according to the manufacturer's protocol. In brief, cells were seeded in sterile 96-well plates and cultured in the medium until they reached a 3×10^4 cells·mL^{-1} concentration (~80% confluence) followed by 24 h of incubation with antimicrobials at 1−100 μM concentrations in a humidified atmosphere at 37 °C with 5% CO_2. The F-12K medium was used for A549 and CHO-K1 cells. SK-MEL-28 cells were

https://doi.org/10.1021/acs.langmuir.3c01008
Langmuir 2023, 39, 12541−12549

incubated in EMEM with 10% FBS and 100 U·mL^{-1} penicillin−streptomycin supplemented with L-glutamine. DMEM used for HeLa cells was additionally supplemented with 2% HEPES (pH 7.4), 0.2 mg·mL^{-1} G418, and 0.1 mg·mL^{-1} hygromycin B. Untreated cells were subject to an equal amount of sterile ultrapure H_2O. After that, the Alamar Blue reagent (10% v/v) was added and incubated for 4 h in the dark. As a positive control, 100% reduced Alamar Blue was prepared by autoclaving 10% v/v reagent in culture media for 15 min before running the assay. Fluorescence signals were collected from nine points per well at three excitation wavelengths (530, 545, and 560 nm) with an emission wavelength of 590 nm using a SpectraMax M5 microplate reader (Molecular Devices, San Jose, CA).

The level of reduced resazurin was calculated as follows

$$\begin{aligned}\text{Red. (\%)} = &(\text{experimental RFU value}\\ &- \text{negative control (medium) RFU value})\\ &/(\text{positive control RFU value}\\ &- \text{negative control (medium) RFU value}) \times 100\end{aligned}$$

Cell viability was estimated as a ratio of the experimental RFU value to the RFU value of untreated cells.[16] The half-maximal inhibitory concentrations (IC_{50}) were identified as antimicrobial concentrations at which the population of viable cells was reduced by 50%, using GraphPad Prism 8.3.1 (logistic nonlinear regression).

Immunofluorescence Microscopy. Cells were grown on glass coverslips until 60−80% confluence followed by washing thrice in phosphate-buffered saline (PBS) and then fixed with 10% formalin (∼4% paraformaldehyde) (Electron Microscopy Sciences, Hatfield, PA). Non-specific protein−protein interactions were blocked with 3% bovine serum albumin (BSA) (Millipore Sigma, Burlington, MA) in PBS, and cell surfaces were immunostained without permeabilization using mouse anti-GD3 primary monoclonal antibody (mAb) (1:80, Abcam, Eugene, CA) according to the manufacturer's protocol or mouse anti-GM3 mAb (1:250, Amsbio LLC, Cambridge, MA) in 2% BSA/PBS for 1 h at room temperature. The secondary antibodies used were goat anti-mouse IgG conjugated to Alexa Fluor 594 and 488 (Invitrogen, Carlsbad, CA, USA) at a concentration of 1:200 in 2% BSA/PBS for 1 h at room temperature followed by extensive washes in PBS. The coverslips were then extensively washed in PBS and mounted onto glass slides (Thermo Fisher Scientific, Waltham, MA) using the Prolong Diamond antifade mountant (Invitrogen, Carlsbad, CA) with 4′,6-diamidino-2-phenylindole (DAPI) for nuclei staining and left to set overnight in the dark prior to sealing. Immunostained cells were imaged with an LSM 800 Zeiss confocal microscope (Thornwood, NY) using 40× and 63× magnification objectives. For statistical analysis, a set of micrographs were collected for each cell line with identical image acquisition settings and exposure times. The data collected were processed using ImageJ[18] software v. 1.52 (National Institute of Health, Bethesda, MD). The corrected total cell fluorescence (CTCF) over the area unit was quantified using the following formula

$$\text{CTCF} = \frac{A \times \text{MFI (cell)} - A \times \text{MFI (background)}}{A}$$

where A indicates the total area of cells selected; MFI refers to the mean fluorescence intensity. Analysis of variance (ANOVA) was performed followed by a Tukey's multiple-comparison test in GraphPad Prism 6.0 (GraphPad Software, Inc., San Diego, CA).

Constant-Pressure Insertion Assays. Langmuir monolayers composed of dipalmitoyl-*sn*-glycero-3 phosphatidylcholine (DPPC) and 1,2-dihexadecanoyl-*sn*-glycero-3-phosphatidylserine (DPPS) were employed to reconstitute plasma membrane of healthy eukaryotic cells, while cancer cell surfaces were modeled using DPPC/GM3 and DPPC/GD3 mixtures at a 7:3 molar ratio. The instrumental setup consisted of a custom-made Teflon Langmuir trough equipped with a movable Teflon barrier controlled for the reversible compression and expansion of monolayers. The surface pressure at the air−water interface was measured by a stationary Wilhelmy plate (Riegler & Kirstein, Potsdam, Germany) and kept invariable via a pressure-area feedback loop throughout the duration of the experiment. Dulbecco's phosphate-buffered saline (Invitrogen, Carlsbad, CA) without Ca^{2+} and Mg^{2+} was used as a subphase, with the temperature being maintained at 22 ± 0.5 °C. To reduce fluctuations and maintain stability, the entire equipment was mounted onto a vibration isolation stage (Newport Corporation, Irvine, CA).

Pre-mixed lipids were deposited onto the aqueous surface from the organic solvent, allowed to evaporate, and then slowly compressed at the surface pressure of 30 mN·m^{-1}, consistent with the lateral pressures in natural cell membranes.[19] MAG2 and OAK stock solutions dissolved in ultrapure water were then injected evenly into the subphase underneath the monolayer up to the final concentration of 10 μM using a micro-syringe with an "L-shaped" needle (VDRL, needle; Hamilton Robotics, Reno, NV). As the injected antimicrobials start interacting with the lipid monolayer, the surface pressure rises, resulting in the barrier expanding the film area to maintain a constant pressure. Knowing the amount of material deposited, the relative change in area per individual lipid molecule ($\Delta A/A$) can be calculated.

Synchrotron X-ray Reflectivity. X-ray measurements were carried out before and after the introduction of antimicrobials using a liquid surface spectrometer at the 9-ID-B (XSD) and 15-ID-C (ChemMatCARS) beamlines at the Advanced Photon Source, Argonne National Laboratory. A Langmuir trough was mounted in a hermetic helium-filled chamber. Low oxygen levels were maintained in the chamber to minimize background scattering. The wavelength (λ) was selected by a cryogenically cooled double-crystal Kozhu monochromator to be 0.92017 Å (1.2374 Å at 15-ID-C beamline). The incident X-ray beam strikes the horizontal surface of the liquid sample at low angle α, close to the critical angle for this wavelength. The scattered beam makes an angle β to the surface and an azimuthal angle ψ to the plane of incidence. In specular X-ray reflectivity geometry, $\alpha = \beta$ and $\psi = 0$, and the intensity of the reflected beam is measured as a function of the incident angle over the wave vector transfer $q_z = (4\pi/\lambda)\sin(\alpha)$ along the surface normal. The background subtraction was done by collecting off-specular signals at fixed distances from the incidence plane. The range of measured angles corresponded to q_z values from approximately 0.01 to 0.7 Å^{-1}.[20] All reflectivity measurements were conducted by translating the trough by 1 mm after the low, mid, and high angle measures, corresponding to q_z ranges of 0.01−0.1, 0.1−0.5, and 0.5−0.7 (Å^{-1}), respectively, to prevent damage from the X-ray beam. All measurements were averaged over three independent measurements.

X-ray Reflectivity Data Analysis. Biologically interacting systems such as those in our work are challenging to model since they do not necessarily adhere to the simplified, though precise "box model" criteria. Our models are mixtures of non-crystalline lipids with variable lengths of soluble sugars that are not fixed in space. Into this system, antimicrobials are introduced that can differentially intercalate into one or more areas of the lipid monolayer. At the same time, the introduction of these surface-active compounds causes an increase in the area occupied by the film. This is caused by the feedback mechanism set to maintain the surface pressure by adjusting the area. In these cases, roughness estimates can be large with respect to layer thickness and the electron density can have a non-Gaussian distribution over the layer thicknesses. Under such circumstances, fitting X-ray reflectivity data using simple models is quite challenging. We chose to analyze our data using the "model-independent fitting" routine in the software StochFit.[21] Here, we started with a guess of the total film thickness, estimated using the first minimum from the reflectivity curves, and a guess of the average film electron density—we assumed 1.0 (ρ/ρ_{water}). This profile was broken into a single box per Å of length, where each box has a fixed thickness. Each box then has a density and smoothing parameter. This film is modeled by assuming that the areas outside of the film have a known, fixed density for the superphase (the air above the film, assumed to have $\rho/\rho_{water} \approx 0$), and the subphase (the water below the film, assumed to have ρ/ρ_{water} of 1.0). Although these thin, biological films are not strongly absorbing materials, absorption is considered by linking the

https://doi.org/10.1021/acs.langmuir.3c01008
Langmuir 2023, 39, 12541−12549

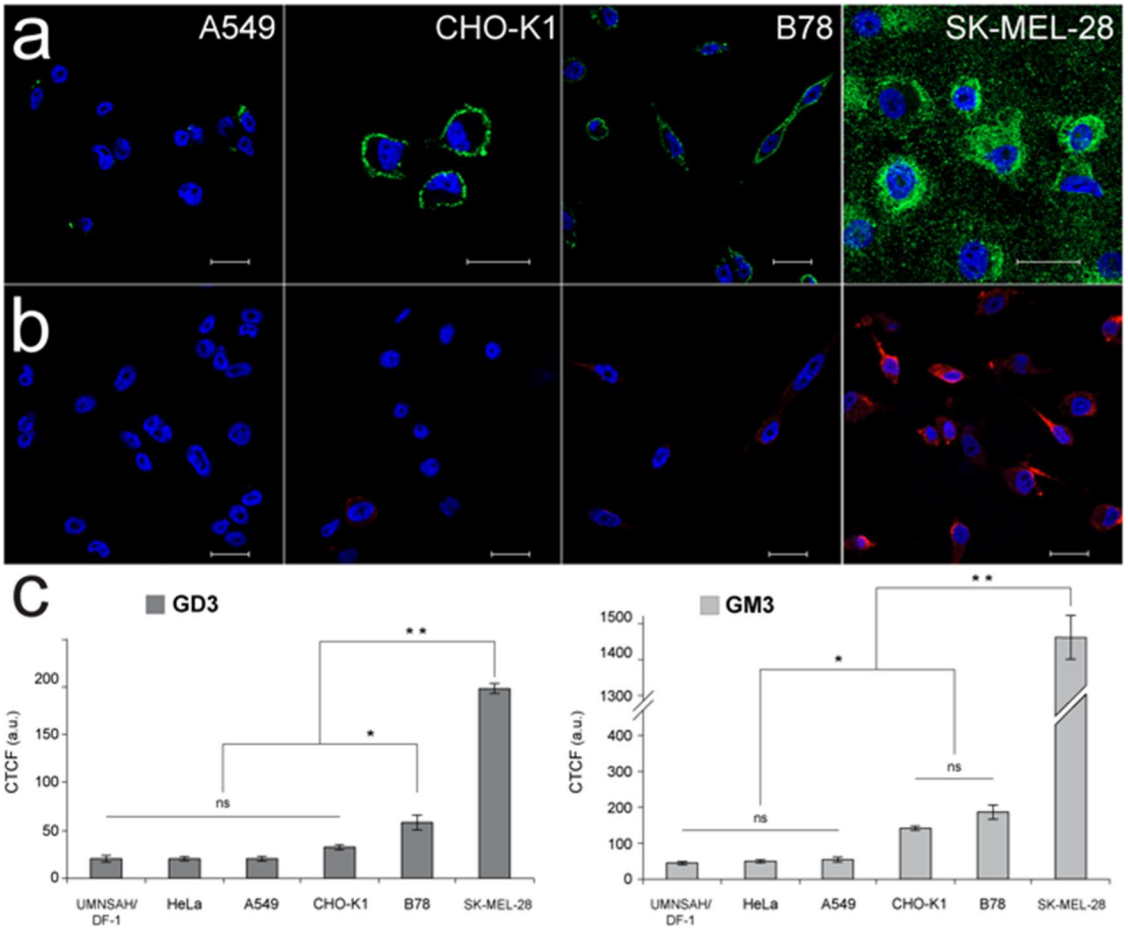

Figure 2. Surface localization of (a) GM3 (green) in cells immunostained with mouse anti-GM3 mAb clone GMR6, IgM, and Alexa Fluor 488 and (b) GD3 (red) labeled with mouse anti-GD3 mAb clone R24, IgG3, and Alexa Fluor 594. Nuclei are stained with DAPI (blue). The scale bar corresponds to 20 μm. (c) The bar graphs quantify the CTCF per μm^2 for each ganglioside. Data represented as mean ± standard error of the mean. Comparison made between the median CTCF values from 10 micrographs of at least 20 cells per each (**$p < 0.001$, *$p < 0.05$). ns—not significant ($p > 0.05$).

absorption profile to the calculated electron density profile; this procedure is detailed by Danauskas et al.[21] and prevents overemphasis and overfitting to the absorption parameters. This assumption reduces to essentially a "first-order" correction where we suspect that the absorption does not vary significantly throughout the film. Each point in the density profile is treated as a layer, and the reflectivity is then calculated by iterating through each of the points of the density profile. Each fit was performed three times using different fitting methods—greedy search, simulated annealing, and stochastic tunneling—to make sure that the final density profile converged to the same solution. After fitting, we are left with a continuous curve of density for each film, with and without the drug present.

To analyze these continuous distributions, we fit the electron density distribution to the standard error function "slabs" using the constraint that the total area under the curves was the same and that this was done using the smallest number of "slabs" possible to make sense of the system. We used 2 for the simple DPPC/DPPS system, since these have been used before, and then 3 for the GM3/GD3 systems, since we expect some additional structure beyond the PC-/PS-like systems (Figure 1). The after profiles were fit using the same number of slabs as the layers before the interaction. These curves are presented in Figure 5B. Analysis of the electron densities involves calculating the number of electrons per unit volume. The density is given by the curves, but the area of the film changes. To visualize the changes in the film, the density curves are normalized to the change in film area (Figure 5, right). The difference between the two area-normalized curves shows where the changes in density occur in the film. These are an oversimplification and are only used for visualization purposes. All analysis is conducted using the derived slabs.

Calculation of the Lipid-to-Drug Ratio. This was done as previously described for other antimicrobials interacting with lipid monolayers.[22−24] In brief, the number of electrons in each slab was calculated using the density and area for both before and after fits. The number of electrons in the antimicrobial was then calculated from the chemical formula. The difference was calculated under the assumption that no additional water is added to the head region since this cannot be known and may be different from film to film. However, the straight difference for the hydrophobic tail region should have no water molecules, and the difference should correspond well to the change in density and area. The lipid-to-drug ratio was then simply calculated by the ratio of the number of electrons in the antimicrobial to the number of excess electrons that are assumed to not be water. This gives a rough estimate of the lipid-to-drug ratio but relies on the assumption that the differences are spread evenly over the beam area and the area per lipid molecule. This may not necessarily be true in all cases but offers a way to apply a similar approach to all films.

RESULTS AND DISCUSSION

Ganglioside Surface Localization. Cells are immunostained without prior permeabilization to evaluate the surface expression of GM3 and GD3 gangliosides. GM3 is abundantly present in both melanomas and CHO-K1 cells with only sporadic surface distribution in human carcinoma and primary

https://doi.org/10.1021/acs.langmuir.3c01008
Langmuir 2023, 39, 12541−12549

Table 1. IC_{50} Values (μM) ± S.D. of MAG2 and OAK[a]

	GM3−			GM3+		
	non-cancer	carcinomas		non-cancer	melanomas	
	UMNSAH/DF-1	HeLa	A549	CHO-K1	B78	SK-MEL-28
MAG2	>100	>100	>100	>100	>100	>100
OAK	86.6 ± 1.9	87.9 ± 2.7	95.8 ± 2.9	26.2 ± 0.8	34.3 ± 1.3	13.6 ± 1.0

[a]Error bars represent S.E.M. obtained from triplicate.

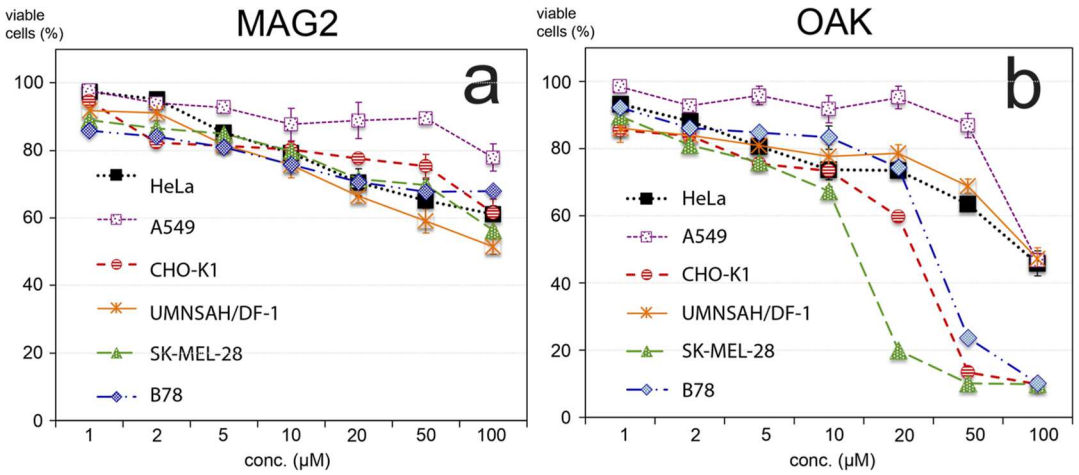

Figure 3. Cell viability curves as measured by Alamar Blue (resazurin) assays for (a) MAG2 and (b) OAK. Cells are incubated in the presence of various drug concentrations (1−100 μM) for 24 h at 37 °C. The percentage of viable cells is calculated as a ratio of the mean fluorescence from cells treated with antimicrobials to the non-treated controls. Error bars represent standard deviation (S.D.) from triplicated measurements.

fibroblasts (Figures 2a and S1). SK-MEL-28 and B78 display elevated levels of GD3 as compared to non-melanoma cell lines (Figure 2b), characterized by a three- to tenfold increase in the signal intensity (Figure 2c).

In Vitro Cytotoxicity. OAK and MAG2 reduce cell viability in a dose-dependent manner. The activity of MAG2 is poor, with IC_{50} > 100 μM for all cell types being investigated (Table 1). Furthermore, the viability of UMNSAH/DF-1 at high concentrations of the peptide is lower (52%) than those for immortalized cell lines (56−78%), indicating poor cell specificity (Figure 3a). OAK displays a comparable cytotoxic effect to MAG2 on adenocarcinoma while providing a better survival rate for primary fibroblasts (IC_{50} ∼ 86.6 μM). A sharp decline in cell viability is observed in both human and mouse melanoma cell lines at concentrations between 10 and 50 μM for OAK but not MAG2 (Figure 3b). The half-maximal inhibitory dose of OAK varies from 13.6 to 34.3 μM, with the best activity being against SK-MEL-28 (Table 1). Interestingly, OAK is also more cytotoxic to non-cancerous CHO-K1 cells presenting elevated GM3 levels than MAG2. A comparative analysis of cell susceptibility toward 50 μM antimicrobials is presented in Figure 4. Fluorescence microscopy data indicate changes in cellular morphology caused by antimicrobials with OAK at concentrations above IC_{50} to induce the loss of membrane integrity and interfere with chromatin organization (Figure S2).

Model Membrane Insertions. The introduction of MAG2 to the DPPC/DPPS monolayer up to the subphase concentration of 10 μM results in minor changes in area per individual lipid molecule (<2%), indicating limited membrane interactions. In turn, the modest area increase of ∼8.5% is induced by OAK. In turn, both antimicrobials readily intercalate into DPPC/GM3 and DPPC/GD3 characterized

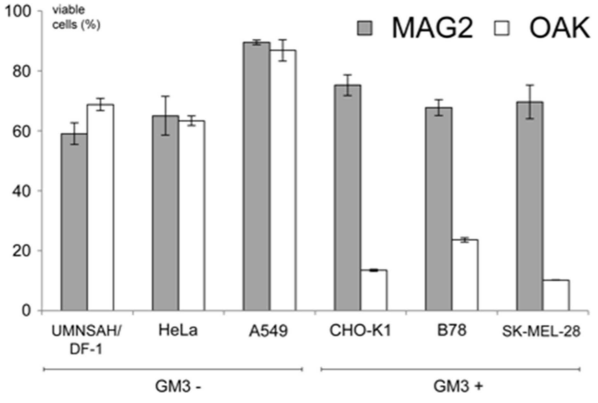

Figure 4. Cell viability after treatment with 50 μM either MAG2 (light gray) or OAK (white). Data are obtained from three independent experiments each sampled in duplicate ± S.D.

by a 4- and 7-fold increase in area expansion by MAG2 and 1.5- and 3.5-fold—for OAK, for mono- and disialoganglioside, respectively (Table 2). It should be noted that local concentrations of antimicrobials at the monolayer surface might differ upon adsorption from the subphase. The selected concentrations to work with are based on the previously published data from in vitro and mechanistic studies.[25] OAK binding affinity constants to POPC/POPG model membranes have been previously found to be ∼2×10^6 $M^{-1}\cdot s^{-1}$,[26] which is comparable to those for magainin 2 ($0.5-1 \times 10^6$ $M^{-1}\cdot s^{-1}$).[27]

Phospholipid monolayers are typically modeled as a stack of several slabs each with a distinct electron density. The upper region closest to the air−water interface (slab 1) corresponds to the hydrocarbon chains of lipids with the electron densities ranging from 0.29 to 0.32 $e^{-}\cdot Å^{-3}$. These values are in line with

https://doi.org/10.1021/acs.langmuir.3c01008
Langmuir 2023, 39, 12541−12549

Table 2. Slab-Modeled X-ray Reflectivity Data[a]

	Slab 1		Slab 2		Slab 3		area per lipid (Å^2)	lipid-to-drug ratio
	length (Å)	density (e^-·Å^{-3})	length (Å)	density (e^-·Å^{-3})	length (Å)	density (e^-·Å^{-3})		
DPPC/**DPPS**	15.61 ± 0.2	0.32 ± 0.03	10.52 ± 0.01	0.45 ± 0.04			44.4 ± 0.2	
+Mag2	15.54 ± 0.02	0.32 ± 0.02	10.49 ± 0.01	0.45 ± 0.04			45.2 ± 0.5	>25
+OAK	14.05 ± 0.01	0.31 ± 0.01	12.72 ± 0.02	0.41 ± 0.01			48.2 ± 0.5	>25
DPPC/**GM3**	15.06 ± 0.02	0.29 ± 0.03	11.96 ± 0.02	0.37 ± 0.10	7.871 ± 0.02	0.35 ± 0.05	50.0 ± 0.4	
+Mag2	14.21 ± 0.01	0.30 ± 0.02	12.59 ± 0.01	0.39 ± 0.05	9.315 ± 0.02	0.35 ± 0.08	54.2 ± 0.5	13
+OAK	13.59 ± 0.02	0.31 ± 0.02	14.03 ± 0.01	0.40 ± 0.01	9.782 ± 0.01	0.36 ± 0.01	55.8 ± 0.5	7
DPPC/**GD3**	14.96 ± 0.01	0.31 ± 0.02	10.51 ± 0.01	0.40 ± 0.01	11.76 ± 0.01	0.36 ± 0.03	46.4 ± 0.1	
+Mag2	13.82 ± 0.02	0.29 ± 0.02	15.32 ± 0.01	0.41 ± 0.10	11.83 ± 0.01	0.38 ± 0.05	52.7 ± 0.6	14
+OAK	8.375 ± 0.04	0.22 ± 0.02	19.81 ± 0.01	0.39 ± 0.04	10.09 ± 0.02	0.36 ± 0.04	60.3 ± 0.5	4

[a]Subscripts: 1—hydrocarbon chains/"tails"; 2—phosphate/sphingosine and carbohydrate "heads"; 3—sialic acid groups.

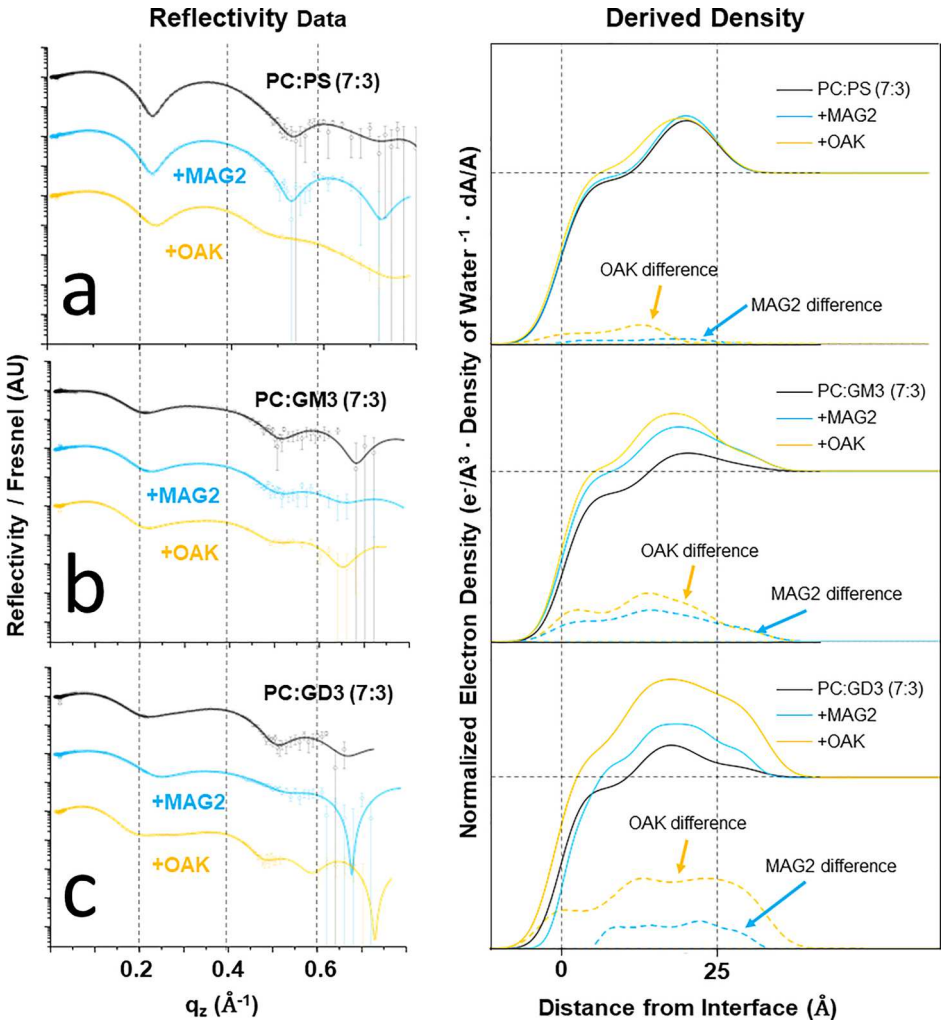

Figure 5. X-ray reflectivity data on monolayers upon interaction with MAG2 (blue) and OAK (orange). (a) Reflected intensities (R) normalized over the Fresnel reflectivity (RF) for an ideally flat air−water interface. Curves are vertically shifted for clarity. The scatter plots show the measured values, where vertical bars indicate the error assuming Poisson distributions about the counted intensity. The solid−line curves are the best fit to the experimental data. (b) Electron density profiles derived from the data in panel (a). Z denotes the distance from the top of the upper slab (slab 1) corresponding to the air−water interface. The electron density distribution by inserted antimicrobials is shown in dashed lines below each set of curves. The density curves are normalized to both the density of water and the change in the film area.

prior measurements of packed acyl chains measured using X-ray reflectivity.[20,28] The subjacent layer (slab 2) peaks in electron density above 0.45 e^-·Å^{-3} from anionic phosphate groups. In monolayers containing GM3 and GD3 gangliosides, slab 2 has lower electron densities of 0.37−0.4 e^-·Å^{-3} contributed by the glucose and galactose residues. An additional slab of the sialic acid group electron subphase (slab 3) is characteristic for DPPC/GM3 and DPPC/GD3

https://doi.org/10.1021/acs.langmuir.3c01008
Langmuir 2023, 39, 12541−12549

monolayers, with the electron densities just slightly above the one of the aqueous buffer (0.334 $e^{-}\cdot Å^{-3}$) (Table 2). X-ray reflectivity on planar lipid monolayer did not reveal the formation of nanotube structures previously described for giant unilamellar vesicles of POPC with GM1.[29] This could be explained by the lack of the curvature effect to achieve a Langmuir model system as well as limited X-ray penetration depth.

The reflectivity profile of DPPC/DPPS does not undergo any notable changes upon introduction of MAG2, indicating little to no permeation into the monolayer (Figure 5a). OAK interacts with outer phosphate groups of lipids without inserting into the hydrophobic core, characterized by an increase in the electron density of slab 2 and the reduced density of slab 1. The lipid-to-drug ratio corresponds to the number of lipids per inserted molecule of the antimicrobial compound and, thus, is inversely proportional to its insertion rate. The high lipid-to-drug ratio (>25) confirms the limited incorporation of antimicrobials into the DPPC/DPPS monolayer. While the increase in area per lipid molecule upon insertion of MAG2 and OAK into DPPC/GM3 is moderate (8−12%), additional electron density contributed to all three slabs indicates them to permeate throughout the entire monolayer. This is also confirmed by the reduced thickness of the lipid film by 1.2 and 2.5 Å, respectively. The peaked density of the DPPC/GM3 monolayer is shifted toward the interface by intercalation of antimicrobials (Figure 5b). In turn, the electron densities mainly contribute to the middle portion of the DPPC/GD3 monolayer characterized by the notable increase in thickness of slab 2 (1.5- and 2-fold for MAG2 and OAK, respectively). OAK tends to insert into both ganglioside-containing monolayers more efficiently than peptide, characterized by a 2- to 3.5-fold lower lipid-to-drug ratio (Table 2).

Result Interpretation. Various tumors, including sarcomas,[30,31] melanomas,[32] lymphomas,[33] and leukemia,[34] exhibit elevated levels of GM3 and GD3 gangliosides. GD3 is often identified as a cancer-specific cell surface antigen in human melanoma.[35] The murine B78 melanoma cell line primarily exhibits GM3 as its sole detectable ganglioside,[36] comparable to non-cancerous CHO-K1 cells, which cannot convert GM3 to GD3 due to the absence of α-2,8-sialyltransferase.[37]

MAG2's cytotoxicity is moderately influenced by the peptide concentration and is possibly the result of non-specific interactions with membrane lipids.[17,38] Although cancer cells often expose phosphatidylserine on their surface,[39] X-ray reflectivity data suggests its insignificant role in melanoma recognition by antimicrobials. MAG2's higher insertion levels into ganglioside-containing monolayers versus DPPC/DPPS can be partially attributed to non-specific electrostatic binding to gangliosides' larger carbohydrate moieties. Hydrophobic forces might also promote the partitioning of the amphipathic peptide α-helix between the membrane's hydrophobic core and polar outer layer.

OAK's recognition of GM3 and GD3 is dictated by specific interactions with sialic acids, elucidating peptidomimetics' cytotoxicity against CHO-K1 and melanoma cells but not primary fibroblasts. Our results from X-ray reflectivity show that the binding constant of OAK to DPPC/GD3 and DPPC/GM3 monolayers is larger than that to the DPPC/DPPS monolayer and larger than those of MAG2. In the interactions of OAK and MAG2 with DPPC/GD3 and DPPC/GM3 monolayers, the fractional area change values are significantly high, indicative of strong peptide−lipid interactions. However, this might not necessarily translate to similar observations in lipid bilayers due to critical area strain and potential pore formation.[40]

The additional sialic acid group in GD3 gangliosides allows OAK's flexible acyl chains to penetrate the carbohydrate moieties of model cancer membranes. However, in lipid bilayers, if the fractional area change surpasses ∼0.05, pore formation can occur due to membrane tension, although this value can depend on the types of lipids and the phase of lipid bilayers.[40] This discrepancy is one of the limitations of our monolayer experiments. Despite this limitation, our work suggests that OAK interacts with GM3- and GD3-enriched lipid membranes, but the precise mechanism of interaction leading to cell death remains undetermined. Although we suspect that OAK might act through a standard mechanism such as the detergent-like (carpet) mode of action or toroidal pore formation, as suggested for MAG2,[41] we cannot confirm this.

Several mechanisms of peptide-induced pore formation have been proposed, such as the MAG2-induced pore formation, where the rate constant of pore formation increases with an increase in the fractional area change of the lipid bilayer due to the binding of MAG2 to the outer monolayer leaflet. This results in increased membrane tension in the inner monolayer, inducing membrane instability and leading to pore formation.[42] When the fractional area change is 0.04, the rate constant of pore formation is extremely high, though this value inducing significant pore formation depends on the types of lipids. Future experiments using methods like NMR,[43] crystallography,[44] circular dichroism,[45] electron microscopy,[46] surface plasmon resonance,[47] and molecular dynamics simulations[48] might offer a clearer understanding of OAK's specific mechanism against cancer cells.

Beyond membrane disruption, our fluorescence data hints that peptidomimetics might exert additional effects, such as DNA binding, reported earlier for OAKs that bind bacterial DNA.[5,49] OAK appears to bind to GM3 and GD3 lipid monolayers, causing a dose-dependent decrease in cell viability. Despite OAK's antimicrobial peptide origins suggesting potential cellular lysis, it remains uncertain whether membrane disruption or other effects cause cell death. Proving that OAKs are lytic against these cancer cells rather than, perhaps, causing cell death due to stress from destabilizing the membrane potential requires additional investigation, which could involve the proposed OAK-induced leakage experiments from lipid vesicles containing GM3, GD3, or PS.[50]

GM3 and GD3 gangliosides' overexpression in malignant melanoma highlights their potential as cancer therapy targets. To enhance our understanding of OAKs' anticancer selectivity, future research should explore their interactions with modified sialic acids, like *N*-glycolylneuraminic acid and O-acetylated derivatives.[51,52] We suggest that identifying glycosylated epitopes on malignant tumor cells as potential targets for antimicrobial peptide mimics could guide the development of next-generation therapeutics.

CONCLUSIONS

Our study provides compelling evidence that OAK mimics' host defense peptides exhibit in vitro activity against melanoma cells expressing GM3 and GD3 gangliosides. X-ray scattering data suggest that peptidomimetics intercalate into sialo-oligosaccharides of glycosylated lipid monolayers. These

https://doi.org/10.1021/acs.langmuir.3c01008
Langmuir 2023, 39, 12541−12549

findings provide insights into their dual mechanism of action that involves a carpet-like demolition of cancer cell membranes and intracellular targeting. Our results highlight the significance of glycosylation in the development of novel targeted therapies to cure melanoma and other malignant tumors and introduce oligo-acylated lysines as effective anticancer therapeutics.

■ ASSOCIATED CONTENT

Supporting Information

The Supporting Information is available free of charge at https://pubs.acs.org/doi/10.1021/acs.langmuir.3c01008.

Surface localization of GM3 and GD3 labeled in HeLa and UMNSAH/DF-1 cells and morphological changes in B78 cells immunostained for GM3 after incubating with MAG2 or OAK (PDF)

■ AUTHOR INFORMATION

Corresponding Author

David Gidalevitz − *Department of Physics, Center for Molecular Study of Condensed Soft Matter (μCoSM), Pritzker Institute of Biomedical Science and Engineering, Illinois Institute of Technology, Chicago, Illinois 60616, United States;* orcid.org/0000-0002-3620-780X; Email: gidalevitz@iit.edu

Authors

Michael W. Martynowycz − *Department of Physics, Center for Molecular Study of Condensed Soft Matter (μCoSM), Pritzker Institute of Biomedical Science and Engineering, Illinois Institute of Technology, Chicago, Illinois 60616, United States;* Present Address: Department of Biological Chemistry, University of California, Los Angeles, Los Angeles, CA 90095, USA.; orcid.org/0000-0003-0055-230X

Konstantin Andreev − *Department of Physics, Center for Molecular Study of Condensed Soft Matter (μCoSM), Pritzker Institute of Biomedical Science and Engineering, Illinois Institute of Technology, Chicago, Illinois 60616, United States;* Present Address: Department of Infectious Diseases, St. Jude Children's Research Hospital, Memphis, TN 38105, USA

Amram Mor − *Department of Biotechnology and Food Engineering, Technion—Israel Institute of Technology, Haifa 32000, Israel*

Complete contact information is available at: https://pubs.acs.org/10.1021/acs.langmuir.3c01008

Author Contributions

M.W.M. and K.A. contributed equally to this work. D.G. conceived the project. D.G., K.A., and M.W.M. designed and performed X-ray scattering experiments. K.A. designed and performed immunofluorescence and cytotoxicity measurements. M.W.M. and K.A. analyzed X-ray scattering data, A.M. designed and synthesized OAK peptidomimetics, and M.W.M. and K.A. wrote the manuscript with input from all authors. D.G. provided supervision.

Notes

The authors declare no competing financial interest.

■ ACKNOWLEDGMENTS

This research was supported by the Israel Science Foundation grant 1233/18 (A.M.) and NIH R01 AI073892 (D.G.). We are indebted to Mahesh Lingaraju, Christopher Bianchi, Binhua Lin, Mati Meron, Wei Bu, Andrey Ivankin, and Ivan Kuzmenko for their help with X-ray measurements at APS. We are grateful to Fadia Zaknoon for her help with the peptidomimetic synthesis and to Robert A. Lamb for cytotoxicity assays and immunofluorescence measurements. This study used resources of the Advanced Photon Source, a U.S. Department of Energy (DOE) Office of Science User Facility operated for the DOE Office of Science by the Argonne National Laboratory under contract no. DE-AC02-06CH11357. NSF's ChemMatCARS Sector 15 (beamline ID-15-C) is supported by the Divisions of Chemistry (CHE) and Materials Research (DMR), National Science Foundation, under grant number NSF/CHE-1834750.

■ REFERENCES

(1) Sonnino, S.; Mauri, L.; Chigorno, V.; Prinetti, A. Gangliosides as Components of Lipid Membrane Domains. *Glycobiology* **2007**, *17*, 1R−13R.

(2) Yu, R. K.; Tsai, Y.-T.; Ariga, T.; Yanagisawa, M. Structures, Biosynthesis, and Functions of Gangliosides-an Overview. *J. Oleo Sci.* **2011**, *60*, 537−544.

(3) Ravindranath, M. H.; Tsuchida, T.; Morton, D. L.; Irie, R. F. Ganglioside GM3: GD3 Ratio as an Index for the Management of Melanoma. *Cancer* **1991**, *67*, 3029−3035.

(4) Radzishevsky, I. S.; Rotem, S.; Bourdetsky, D.; Navon-Venezia, S.; Carmeli, Y.; Mor, A. Improved Antimicrobial Peptides Based on Acyl-Lysine Oligomers. *Nat. Biotechnol.* **2007**, *25*, 657−659.

(5) Rotem, S.; Radzishevsky, I. S.; Bourdetsky, D.; Navon-Venezia, S.; Carmeli, Y.; Mor, A. Analogous Oligo-Acyl-Lysines with Distinct Antibacterial Mechanisms. *Faseb. J.* **2008**, *22*, 2652−2661.

(6) Sarig, H.; Livne, L.; Held-Kuznetsov, V.; Zaknoon, F.; Ivankin, A.; Gidalevitz, D.; Mor, A. A Miniature Mimic of Host Defense Peptides with Systemic Antibacterial Efficacy. *Faseb. J.* **2010**, *24*, 1904−1913.

(7) Zaknoon, F.; Wein, S.; Krugliak, M.; Meir, O.; Rotem, S.; Ginsburg, H.; Vial, H.; Mor, A. Antiplasmodial Properties of Acyl-Lysyl Oligomers in Culture and Animal Models of Malaria. *Antimicrob. Agents Chemother.* **2011**, *55*, 3803−3811.

(8) Held-Kuznetsov, V.; Rotem, S.; Assaraf, Y. G.; Mor, A. Host-Defense Peptide Mimicry for Novel Antitumor Agents. *Faseb. J.* **2009**, *23*, 4299−4307.

(9) Zaknoon, F.; Sarig, H.; Rotem, S.; Livne, L.; Ivankin, A.; Gidalevitz, D.; Mor, A. Antibacterial Properties and Mode of Action of a Short Acyl-Lysyl Oligomer. *Antimicrob. Agents Chemother.* **2009**, *53*, 3422−3429.

(10) Andreev, K. The Structural Role of Gangliosides: Insights from x-Ray Scattering on Model Membranes. *Curr. Med. Chem.* **2020**, *27*, 6548−6570.

(11) Andreev, K.; Martynowycz, M. W.; Gidalevitz, D. Peptoid Drug Discovery and Optimization via Surface X-Ray Scattering. *Biopolymers* **2019**, *110*, No. e23274.

(12) Andreev, K.; Martynowycz, M. W.; Lingaraju, M.; Bianchi, C.; Mor, A.; Gidalevitz, D. Antimicrobial Peptidomimetics with Activity towards Cancer Cells. *Biophys. J.* **2019**, *116*, 86a.

(13) Blankenberg, F. G.; Katsikis, P. D.; Tait, J. F.; Davis, R. E.; Naumovski, L.; Ohtsuki, K.; Kopiwoda, S.; Abrams, M. J.; Darkes, M.; Robbins, R. C.; et al. *In vivo* detection and imaging of phosphatidylserine expression during programmed cell death. *Proc. Natl. Acad. Sci. U.S.A.* **1998**, *95*, 6349−6354.

(14) Shlomovitz, I.; Speir, M.; Gerlic, M. Flipping the Dogma−Phosphatidylserine in Non-Apoptotic Cell Death. *Cell Commun. Signaling* **2019**, *17*, 139−212.

(15) Gidalevitz, D.; Ishitsuka, Y.; Muresan, A. S.; Konovalov, O.; Waring, A. J.; Lehrer, R. I.; Lee, K. Y. C. Interaction of Antimicrobial

Peptide Protegrin with Biomembranes. *Proc. Natl. Acad. Sci. U.S.A.* **2003**, *100*, 6302−6307.
(16) Brezesinski, G.; Möhwald, H. Langmuir Monolayers to Study Interactions at Model Membrane Surfaces. *Adv. Colloid Interface Sci.* **2003**, *100*−*102*, 563−584.
(17) Lehmann, J.; Retz, M.; Sidhu, S. S.; Suttmann, H.; Sell, M.; Paulsen, F.; Harder, J.; Unteregger, G.; Stöckle, M. Antitumor Activity of the Antimicrobial Peptide Magainin II against Bladder Cancer Cell Lines. *Eur. Urol.* **2006**, *50*, 141−147.
(18) Schneider, C. A.; Rasband, W. S.; Eliceiri, K. W. NIH Image to ImageJ: 25 Years of Image Analysis. *Nat. Methods* **2012**, *9*, 671−675.
(19) Marsh, D. Lateral Pressure in Membranes. *Biochim. Biophys. Acta, Rev. Biomembr.* **1996**, *1286*, 183−223.
(20) Als-Nielsen, J.; Jacquemain, D.; Kjaer, K.; Leveiller, F.; Lahav, M.; Leiserowitz, L. Principles and Applications of Grazing Incidence X-Ray and Neutron Scattering from Ordered Molecular Monolayers at the Air-Water Interface. *Phys. Rep.* **1994**, *246*, 251−313.
(21) Danauskas, S. M.; Li, D.; Meron, M.; Lin, B.; Lee, K. Y. C. Stochastic Fitting of Specular X-Ray Reflectivity Data Using StochFit. *J. Appl. Crystallogr.* **2008**, *41*, 1187−1193.
(22) Martynowycz, M. W.; Rice, A.; Andreev, K.; Nobre, T. M.; Kuzmenko, I.; Wereszczynski, J.; Gidalevitz, D. Salmonella Membrane Structural Remodeling Increases Resistance to Antimicrobial Peptide LL-37. *ACS Infect. Dis.* **2019**, *5*, 1214−1222.
(23) Andreev, K.; Bianchi, C.; Laursen, J. S.; Citterio, L.; Hein-Kristensen, L.; Gram, L.; Kuzmenko, I.; Olsen, C. A.; Gidalevitz, D. Guanidino Groups Greatly Enhance the Action of Antimicrobial Peptidomimetics against Bacterial Cytoplasmic Membranes. *Biochim. Biophys. Acta, Biomembr.* **2014**, *1838*, 2492−2502.
(24) Andreev, K.; Martynowycz, M. W.; Ivankin, A.; Huang, M. L.; Kuzmenko, I.; Meron, M.; Lin, B.; Kirshenbaum, K.; Gidalevitz, D. Cyclization Improves Membrane Permeation by Antimicrobial Peptoids. *Langmuir* **2016**, *32*, 12905−12913.
(25) Matsuzaki, K.; Sugishita, K.; Harada, M.; Fujii, N.; Miyajima, K. Interactions of an Antimicrobial Peptide, Magainin 2, with Outer and Inner Membranes of Gram-Negative Bacteria. *Biochim. Biophys. Acta, Biomembr.* **1997**, *1327*, 119−130.
(26) Sarig, H.; Rotem, S.; Ziserman, L.; Danino, D.; Mor, A. Impact of Self-Assembly Properties on Antibacterial Activity of Short Acyl-Lysine Oligomers. *Antimicrob. Agents Chemother.* **2008**, *52*, 4308−4314.
(27) Gregory, S. M.; Pokorny, A.; Almeida, P. F. F. Magainin 2 Revisited: A Test of the Quantitative Model for the All-or-None Permeabilization of Phospholipid Vesicles. *Biophys. J.* **2009**, *96*, 116−131.
(28) Vaknin, D.; Kjaer, K.; Als-Nielsen, J.; Lösche, M. Structural Properties of Phosphatidylcholine in a Monolayer at the Air/Water Interface. *Biophys. J.* **1991**, *59*, 1325−1332.
(29) Bhatia, T.; Agudo-Canalejo, J.; Dimova, R.; Lipowsky, R. Membrane Nanotubes Increase the Robustness of Giant Vesicles. *ACS Nano* **2018**, *12*, 4478−4485.
(30) Chang, H. R.; Cordon-Cardo, C.; Houghton, A. N.; Cheung, N.-K. V.; Brennan, M. F. Expression of Disialogangliosides GD2 and GD3 on Human Soft Tissue Sarcomas. *Cancer* **1992**, *70*, 633−638.
(31) Dobrenkov, K.; Ostrovnaya, I.; Gu, J.; Cheung, I. Y.; Cheung, N.-K. V. Oncotargets GD2 and GD3 Are Highly Expressed in Sarcomas of Children, Adolescents, and Young Adults. *Pediatr. Blood Cancer* **2016**, *63*, 1780−1785.
(32) Pukel, C. S.; Lloyd, K. O.; Travassos, L. R.; Dippold, W. G.; Oettgen, H. F.; Old, L. J. GD3, a prominent ganglioside of human melanoma. Detection and characterisation by mouse monoclonal antibody. *J. Exp. Med.* **1982**, *155*, 1133−1147.
(33) Merritt, W. D.; Casper, J. T.; Lauer, S. J.; Reaman, G. H. Expression of GD3 Ganglioside in Childhood T-Cell Lymphoblastic Malignancies. *Cancer Res.* **1987**, *47*, 1724−1730.
(34) Anh-Tuan, N.; Pick, J.; Mod, A.; Hollan, S. R. Gangliosides in Acute Myeloid Leukaemia (AML) and Non-Hodgkin's Lymphoma (NHL). *Eur. J. Cancer Clin. Oncol.* **1986**, *22*, 1003−1007.
(35) Dippold, W. G.; Lloyd, K. O.; Li, L. T.; Ikeda, H.; Oettgen, H. F.; Old, L. J. Cell Surface Antigens of Human Malignant Melanoma: Definition of Six Antigenic Systems with Mouse Monoclonal Antibodies. *Proc. Natl. Acad. Sci. U.S.A.* **1980**, *77*, 6114−6118.
(36) Lloyd, K. O.; Gordon, C. M.; Thampoe, I. J.; DiBenedetto, C. Cell Surface Accessibility of Individual Gangliosides in Malignant Melanoma Cells to Antibodies Is Influenced by the Total Ganglioside Composition of the Cells. *Cancer Res.* **1992**, *52*, 4948−4953.
(37) Satake, H.; Chen, H. Y.; Varki, A. Genes Modulated by Expression of GD3 Synthase in Chinese Hamster Ovary Cells: Evidence That the Tis21 Gene Is Involved in the Induction of GD3 9-O-Acetylation. *J. Biol. Chem.* **2003**, *278*, 7942−7948.
(38) Anghel, R.; Jitaru, D.; Bădescu, L.; Bădescu, M.; Ciocoiu, M. The Cytotoxic Effect of Magainin II on the MDA-MB-231 and M14K Tumour Cell Lines. *BioMed Res. Int.* **2013**, *2013*, 831709.
(39) Ran, S.; Downes, A.; Thorpe, P. E. Increased Exposure of Anionic Phospholipids on the Surface of Tumor Blood Vessels. *Cancer Res.* **2002**, *62*, 6132−6140.
(40) Needham, D.; Nunn, R. S. Elastic Deformation and Failure of Lipid Bilayer Membranes Containing Cholesterol. *Biophys. J.* **1990**, *58*, 997−1009.
(41) Cruciani, R. A.; Barker, J. L.; Zasloff, M.; Chen, H.-C.; Colamonici, O. Antibiotic Magainins Exert Cytolytic Activity against Transformed Cell Lines through Channel Formation. *Proc. Natl. Acad. Sci. U.S.A.* **1991**, *88*, 3792−3796.
(42) Karal, M. A. S.; Alam, J. M.; Takahashi, T.; Levadny, V.; Yamazaki, M. Stretch-Activated Pore of the Antimicrobial Peptide, Magainin 2. *Langmuir* **2015**, *31*, 3391−3401.
(43) Yamaguchi, S.; Hong, T.; Waring, A.; Lehrer, R. I.; Hong, M. Solid-State NMR Investigations of Peptide−Lipid Interaction and Orientation of a β-Sheet Antimicrobial Peptide, Protegrin. *Biochemistry* **2002**, *41*, 9852−9862.
(44) Trenker, R.; Call, M. E.; Call, M. J. Crystal Structure of the Glycophorin A Transmembrane Dimer in Lipidic Cubic Phase. *J. Am. Chem. Soc.* **2015**, *137*, 15676−15679.
(45) Bürck, J.; Wadhwani, P.; Fanghänel, S.; Ulrich, A. S. Oriented Circular Dichroism: A Method to Characterize Membrane-Active Peptides in Oriented Lipid Bilayers. *Acc. Chem. Res.* **2016**, *49*, 184−192.
(46) Janson, K.; Kyrilis, F. L.; Tüting, C.; Alfes, M.; Das, M.; Träger, T. K.; Schmidt, C.; Hamdi, F.; Vargas, C.; Keller, S.; Meister, A.; Kastritis, P. L. Cryo-Electron Microscopy Snapshots of Eukaryotic Membrane Proteins in Native Lipid-Bilayer Nanodiscs. *Biomacromolecules* **2022**, *23*, 5084−5094.
(47) Mozsolits, H.; Aguilar, M.-I. Surface Plasmon Resonance Spectroscopy: An Emerging Tool for the Study of Peptide−Membrane Interactions. *Pept. Sci.* **2002**, *66*, 3−18.
(48) Zhao, L.; Cao, Z.; Bian, Y.; Hu, G.; Wang, J.; Zhou, Y. Molecular Dynamics Simulations of Human Antimicrobial Peptide LL-37 in Model POPC and POPG Lipid Bilayers. *Int. J. Mol. Sci.* **2018**, *19*, 1186.
(49) Makobongo, M. O.; Gancz, H.; Carpenter, B. M.; McDaniel, D. P.; Merrell, D. S. The Oligo-Acyl Lysyl Antimicrobial Peptide C12K-2β12 Exhibits a Dual Mechanism of Action and Demonstrates Strong in Vivo Efficacy against Helicobacter Pylori. *Antimicrob. Agents Chemother.* **2012**, *56*, 378−390.
(50) Matsuzaki, K.; Harada, M.; Handa, T.; Funakoshi, S.; Fujii, N.; Yajima, H.; Miyajima, K. Magainin 1-Induced Leakage of Entrapped Calcein out of Negatively-Charged Lipid Vesicles. *Biochim. Biophys. Acta, Biomembr.* **1989**, *981*, 130−134.
(51) Dorvignit, D.; Boligan, K. F.; Relova-Hernández, E.; Clavell, M.; López, A.; Labrada, M.; Simon, H.-U.; López-Requena, A.; Mesa, C.; von Gunten, S. Antitumor Effects of the GM3 (Neu5Gc) Ganglioside-Specific Humanized Antibody 14F7hT against Cmah-Transfected Cancer Cells. *Sci. Rep.* **2019**, *9*, 9921−10012.
(52) Cavdarli, S.; Delannoy, P.; Groux-Degroote, S. O-Acetylated Gangliosides as Targets for Cancer Immunotherapy. *Cells* **2020**, *9*, 741.

https://doi.org/10.1021/acs.langmuir.3c01008
Langmuir 2023, 39, 12541−12549